3D numerical simulation of the VAR consumable electrode melting process

Rayan Bhar, Alain Jardy, Pierre Chapelle, Vincent Descotes

3D NUMERICAL SIMULATION OF THE VAR CONSUMABLE ELECTRODE MELTING PROCESS

R. Bhar[1, 2], A. Jardy[1], P. Chapelle[1] and V. Descotes[2]

[1] Institut Jean Lamour - UMR CNRS 7198, LabEx DAMAS, Université de Lorraine, 2 allée André Guinier, Campus Artem, 54011, Nancy Cedex, France
[2] Aperam Imphy Alloys - Avenue Jean Jaurès, 58160 Imphy, France

Keywords: VAR process, consumable electrode, dripping, liquid metal film, melt rate

Abstract

A 3D numerical model was set-up to simulate the formation and dynamics of the liquid metal film under the consumable electrode during VAR process. In the present paper the implementation of this model is described. It was developed using the open source computational fluid dynamics (CFD) software, OpenFOAM. The model solves coupled momentum and energy equations combined with a volume-of-fluid (VOF) method to track the liquid metal free surface. The melting of the electrode material is modelled with an enthalpy-porosity approach. The electric power supplied by the arc is supposed to be uniform and distributed between the electrode as well as the liquid bath. For a given electric arc power, the model quantitatively predicts the dripping rate, hence the overall melt rate. Simulations are validated through comparisons with experimental data.

Nomenclature

Symbol	Description	Unit
α_m	Metal volume fraction	[-]
g_l	Liquid fraction	[-]
γ	Solid fraction	[-]
σ	Surface tension	[$N.m^{-1}$]
k_c	Curvature	[m^{-1}]
ρ	Density	[$kg.m^{-3}$]
μ	Dynamic viscosity	[$Pa.s^{-1}$]
k	Thermal conductivity	[$W.m^{-1}.K^{-1}$]
cp	Specific heat	[$J.\ K^{-1}.kg^{-1}$]
L	Latent heat of melting	[$J.kg^{-1}$]
h	Total enthalpy	[$J.\ K^{-1}$]
h_{lat}	Latent heat	[$J.\ K^{-1}$]
h_{sen}	Sensible enthalpy	[$J.\ K^{-1}$]
T_{sol}	Solidus temperature	[°C]
T_{liq}	Liquidus temperature	[°C]
λ_2	Secondary dendrite arm spacing	[m]
U	Velocity	[$m.s^{-1}$]

P	Power	[W]
m	Metal	
VOF	Volume Of Fluid	
CSF	Continuum Surface Force	
CFL	Courant-Friedrich-Lewy	
MULES	Multidimensional universal limiter with explicit solution	

Introduction

Vacuum arc remelting (VAR) is a secondary remelting process used to improve cleanliness as well as chemical and mechanical homogeneity of metal ingots. VAR was the first remelting process to be used commercially for superalloys processing. It is also typically the final stage in the melting cycle of reactive metals such as titanium and zirconium alloys. [1]

The process consists of melting a consumable electrode under vacuum (see Fig. 1). The heat source is a DC electric arc of low voltage and high current. The arc is created between the electrode (cathode) and the base plate of a water-cooled copper crucible at the beginning of the melt, then between the electrode and the secondary ingot (anode) forming in the crucible. The melting of the tip of the electrode generates a liquid metal film under the electrode, from which metal drops are produced that fall under the action of gravity into the crucible and progressively solidify to form the secondary ingot. At any instant, the ingot is composed of three zones: the fully solidified metal, the liquid pool fed by metal drops and an intermediate mushy zone.

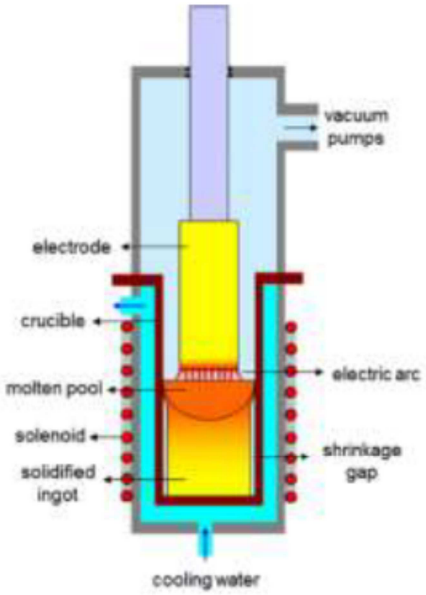

Figure 1. Schematic representation of the vacuum arc remelting process.

The quality of the produced ingots strongly depends on the operating conditions of remelting. Among them, the melt rate and the interelectrode gap play a key role, since they have significant effects on heat transfer conditions at the free surface of the liquid pool, which have important implications on the ingot structure [2].

The VAR process has been investigated previously with both experimental and numerical

approaches. On the experimental side, some studies were devoted to establish various correlations between the operating parameters [3, 4], whereas some research work focused on the electric arc behavior and metal transfer mechanisms in the interelectrode region, which were observed using high speed video cameras in specifically instrumented VAR furnaces [5,6]. Modelling of the VAR process is a difficult task, because the process involves a wide range of coupled physical and chemical phenomena, such as fluid flow, heat and mass transfer, solidification (macro and microsegregation), electromagnetic forces… In the literature, most modelling works deal with the development of Computational Fluid Dynamics (CFD) models of the ingot growth and solidification. The majority of authors considers a 2D axisymmetric geometry of the ingot and solves the conservation equations of mass, momentum and energy, accounting for turbulence phenomena and electromagnetic forces in the liquid pool as well as the solidification of the metal. Examples of such models are the SOLAR code [7] and the MeltFlow-VAR code [8]. A multiscale 3D numerical model of VAR was developed by Pericleous et al. [9], which deals also with the ingot behavior. However, studies of the liquid film formation under the electrode are non-existent in literature.

The present work focuses on the interelectrode gap of the VAR process. The aim is to numerically study the liquid film behavior under the electrode and to predict the melt rate of the electrode for a given electric arc power. A 3D model describing the melting of the consumable electrode and the dynamics of the liquid film formed at the electrode tip was developed using the CFD open source software OpenFOAM. The model considers fluid flow, heat transfer with phase change and the deformation of the free surface of the liquid film. The electromagnetic effects related to the flow of current in the electrode are not yet taken into account. The model is concerned with both large interelectrode gaps, for which the metal transfer results from the formation of molten metal drops from the electrode and their detachment before contacting the ingot, and short interelectrode gaps, for which the metal transfer involves the formation of molten metal bridges (drip-shorts) between the electrode and the ingot. In this paper, we only report results regarding large interelectrode gaps. In section 2, the model is described, including physical and mathematical issues, constitutive equations, boundary conditions and the numerical procedure. In section 3, examples of model results detailing the computed liquid film dynamics and thermal behavior of the electrode during the VAR melt of a small-scale electrode are presented. Finally, conclusions of the present study are drawn in section 4.

Numerical model

The formation and dynamics of the liquid film under the consumable electrode during the VAR process is simulated with a multiphase CFD approach. The metal phase change is accounted for using the enthalpy-porosity method [10] and the shape and position of the free surface of the liquid film are calculated using the volume of fluid (VOF) interface capturing method [11]. Note that in a VAR furnace the liquid metal film is exposed to a low pressure arc plasma. The present model does not deal with the description of this complex latter phase, which is represented here as a neutral gas phase.

Fluid flow and behavior of the free surface

The computed behavior of the free surface of the liquid metal film is based on the VOF approach. In order to identify the metal-gas interface, the model solves an advection equation of the volume

fraction of the metal α_m (either solid or liquid) present in each computational cell:

$$\frac{\partial \boldsymbol{\alpha_m}}{\partial \boldsymbol{t}} + \boldsymbol{\nabla}.(\boldsymbol{U}\boldsymbol{\alpha_m}) + \boldsymbol{\nabla}.\left(\boldsymbol{U_r}\boldsymbol{\alpha_m}(\mathbf{1}-\boldsymbol{\alpha_m})\right) = \mathbf{0} \quad (1)$$

$\alpha_m = 0$ if no metal is present in the cell, $\alpha_m = 1$ for a cell completely filled with metal, and $0 < \alpha_m < 1$ if the interface is present in the cell. In the VOF formulation implemented in OpenFOAM, the volume fraction transport equation contains an additional convective term (third term in Eq. 1), referred to as "compression term". This term compresses the interface by minimizing the numerical diffusion of the volume fraction while ensuring its boundedness. It can be noticed that this additional compression term acts only at the vicinity of the interface region where $\alpha_m(1-\alpha_m) \neq 0$. Therefore, it does not affect the fluid flow outside this region [12].

The gas-liquid metal flow is governed by a single set of continuity and Navier-Stokes equations

- Continuity equation

$$\frac{\partial \boldsymbol{\rho}}{\partial \boldsymbol{t}} + \boldsymbol{\nabla}.(\boldsymbol{\rho U}) = \mathbf{0} \quad (2)$$

- Momentum conservation equation

$$\frac{\partial \rho \boldsymbol{U}}{\partial t} + \boldsymbol{\nabla}.(\rho \boldsymbol{U}\boldsymbol{U}) = -\boldsymbol{\nabla} p + \boldsymbol{\nabla}.(\mu\, \boldsymbol{\nabla}\, \boldsymbol{U}) + \boldsymbol{f_\sigma} + \rho_{ref}(1-\beta(T-T_{liq}))\boldsymbol{g} - \frac{\mu_m}{K}\boldsymbol{U} \quad (3)$$

The thermophysical properties are calculated as volume fraction weighted averages of the properties of the phases present in the cell:

$$\xi = \alpha_m \xi_m + (1-\alpha_m)\xi_{gas} \quad (4)$$

All thermophysical properties are assumed to be independent of the temperature except for the density in the gravitational term (Eq. 3), which is calculated using the Boussinesq approximation. Surface tension effects are taken into account through a continuous equivalent volumetric force $\boldsymbol{f_\sigma}$ (Continuum Surface Force model) as proposed by Brackbill [13]. This force, acting only in the vicinity of the interface and directly linked to the interface curvature k_c, is defined as:

$$\boldsymbol{f_\sigma} = \sigma \frac{2\rho}{\rho_m + \rho_{gas}} k_c\, \boldsymbol{\nabla}\alpha_m \quad (5)$$

A problem encountered in this formulation is the presence of numerical parasitic velocity vortices known as "spurious currents" [14]. These "spurious velocities" appear in the gas phase near the interface despite the absence of any external forces and can be very significant when the capillary effects are predominant. These high velocities force to use very small time steps to maintain the stability of the simulation (CFL criterion), which increases the computational time. In addition, their magnitude does not decrease with neither mesh refinement nor smaller computational time steps [15]. In the current study, a filtration method consisting in setting to zero the velocities of the gaseous phase was implemented to eliminate those spurious velocities.

The last source term on the right hand side of Eq. 3 is derived from the Darcy law. The dendritic mushy zone is treated as a porous medium whose permeability is calculated using the well-known Kozeny-Carman model.

$$K = \frac{\lambda_2^2\,(1-\gamma)^3}{180\,\gamma^2} \quad (6)$$

where γ is the solid fraction in the cell $\gamma = \alpha_m (1-g_l)$. In practice, the effect of this term is as follows. In the fully liquid cells ($\gamma = 0$), the source term is zero and the "classical" Navier-Stokes equation is solved. In the cells where a phase change occurs, the source term dominates over the transient, convective and diffusive terms, thereby forcing to imitate the Kozeny-Carman model [10]. In the fully solid cells ($\gamma = 1$), the source term swamps out all other terms in the momentum equation, which forces velocities to zero [16].

Heat transfer with phase change

The enthalpy-porosity method is based on the enthalpy formulation of the energy conservation equation:

$$\frac{\partial(h)}{\partial t} + \boldsymbol{\nabla}.(h\boldsymbol{U}) = \boldsymbol{\nabla}.(k\,\boldsymbol{\nabla}\,T) \tag{7}$$

The enthalpy may be computed as the sum of sensible enthalpy and latent heat absorbed when the metal changes from solid to liquid. The total enthalpy is given by:

$$h = \int_{T_{ref}}^{T} \rho C_p dT + \rho_m \alpha_m g_l L \tag{8}$$

The energy conservation may thus be expressed as follows:

$$\frac{\partial(\rho C_p T)}{\partial t} + \boldsymbol{\nabla}.(\rho C_p T\boldsymbol{U}) = \boldsymbol{\nabla}.(k\,\boldsymbol{\nabla}\,T) - \rho_m L\left(\frac{\partial \alpha_m g_l}{\partial t} + \boldsymbol{\nabla}.(\alpha_m g_l \boldsymbol{U})\right) + P_{arc} \tag{9}$$

The second term on the right hand side of Eq. 9 accounts for the evolution of the latent heat during phase change. The liquid-solid interface is not tracked explicitly. Instead, the melting zone is treated as a porous zone as described previously, in which the liquid fraction lies between 0 and 1. The liquid fraction is a function of temperature and can be, for example, calculated as follows:

$$\begin{cases} g_l = 0 & if\ T < T_{sol} \\ g_l = 1 & if\ T > T_{liq} \\ g_l = \dfrac{T - T_{sol}}{T_{liq} - T_{sol}} & if\ \ T_{sol} < T < T_{liq} \end{cases} \tag{10}$$

The last term on the right hand side of Eq. 9 is the thermal power provided by the electric arc to the metal. In fact, this power corresponds to a boundary condition of the problem, which is treated here as a volumetric source term applied only in the cells crossed by the metal/gas interface (defined as the cells where $\alpha_m = 0.5$). The total arc power P_{tot} is assumed to be uniformly distributed at both the electrode base and the ingot top surface, which leads to the following expression of P_{arc}:

$$P_{arc} = \frac{P_{tot}}{\sum S_i}\frac{S_i}{V_{ci}} \tag{11}$$

where V_{ci} is the volume of the cell (crossed by the interface) i, S_i is the area of the portion of the interface contained in cell i and $\sum S_i$ is the total area of the interface.

Boundary conditions

The main boundary conditions of the model are outlined here based on the dependent variables

under consideration, i.e. velocity, pressure and temperature.

- Velocity: A no-slip boundary condition is used at walls.
- Pressure: A pressure outlet boundary condition is used at outlets.
- Temperature: The walls are adiabatic, which results in a zero temperature gradient condition. The temperature is fixed (ambient) at the electrode top.

Numerical aspects

The pressure-velocity coupling is handled by the PIMPLE algorithm (combination of the PISO [17] and SIMPLE [18], algorithms). The convective terms in the conservation equations are discretized with a second order VanLeer scheme while the diffusion terms are central differenced. The model is based on the existent multiphase flow solver InterFoam using the MULES correction.

Example of simulation results

The numerical model described above was applied to simulate the melt of a small diameter Ti electrode with a large interelectrode gap performed experimentally by Chapelle et al. [6].

Fig. 2 shows a vertical cut of the computational domain with the initial metal represented in yellow. The electrode diameter is 160 mm, its height is 150 mm and the interelectrode gap is 60 mm. The total electric arc power is 76.8 kW, which is uniformly distributed between the electrode and liquid pool as schematized in the Fig. 2 by red lines. Initially, the metal is in solid state with a temperature of 300 K. As stated above, all the walls are supposed thermally insulated except the top boundary on which the temperature is fixed to 300 K. The computational grid is a uniform structured mesh consisting of around 2.5 million cells.

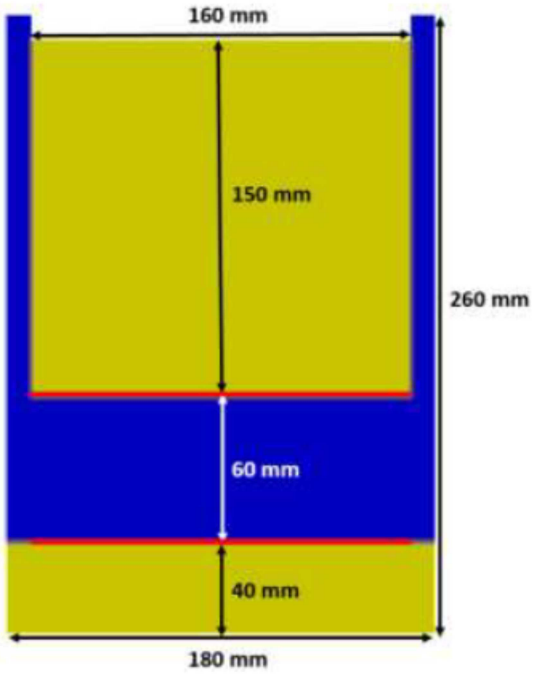

Figure 2. Dimensions and initial state of the simulated system.

The thermophysical parameters used for the simulation are reported in Table 1.

Parameters	Value		Unit
	Titanium	Gas	
Density p	4208	0,2	$kg.m^{-3}$
Kinematic viscosity v	$1.16 X 10^{-6}$	$2.72 X 10^{-4}$	$m^2.s^{-1}$
Surface tension a	1.56		$N.m^{-1}$
Specific heat c_p	554	1237	$].kg^{-1}K^{-1}$
Thermal conductivity il	22	$9,55.10^{-2}$	$W.m^{-1}.K^{-1}$
Dilatation coefficient f3	$8.90 X 10^{-6}$	0	K^{-1}
Liquidus temperature T_{liq}	1703	-	°C
Solidus temperature T_{sol}	1653	-	°C
Reference temperature T_{ref}	1703	-	°C
Latent heat of melting L	$3.65 X 10^5$	-	$].kg^{-1}$

Table 1. Thermophysical parameters used for the simulation.

Liquid film behavior

At the initial state, the system is isothermal. The thermal power provided by the electric arc heats the electrode. At this stage, the heat transfer is purely conductive. As soon as the temperature of the tip reaches the solidus temperature, the electrode starts to melt and a distorted liquid film, whose thickness is about few millimeters, is formed. Owing to the Rayleigh-Taylor instability which occurs when a heavy fluid is placed above a lighter one in a gravitational field [19], small protuberances appear and are spatially distributed in lattices as shown in Fig. 3, which gives the depth reached by the protuberances in the liquid film. Continuous feeding of the film due to the metal melting eventually destabilizes these structures. The protuberances are subject to horizontal movements. Once they get close to each other, they coalesce, grow and form drops. Such a behavior is qualitatively consistent with the theory of Limat et al. [20].

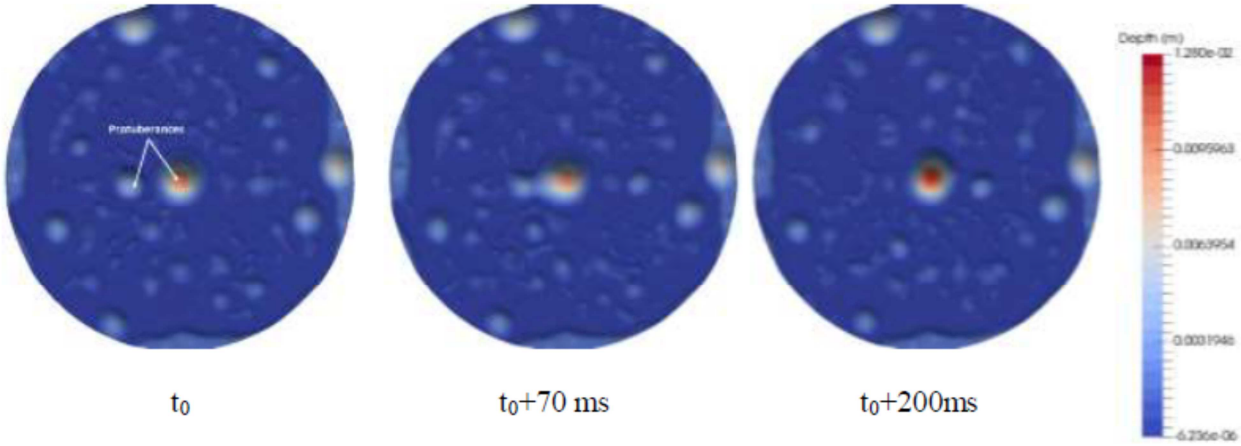

Figure 3. Depth of protuberances formed from the liquid film.

The successive growth, elongation and detachment stages of a drop are compared in Fig. 4 with the experimental observations reported by Chapelle et al [6]. On the left image, the protuberance which grows by drainage of the liquid metal has a cylindrical shape. Then it stretches resulting in the formation of a drop. The drop remains attached to the liquid film by a filament which gradually becomes thinner. This latter process eventually triggers the break-up of the filament and subsequent detachment of the drop.

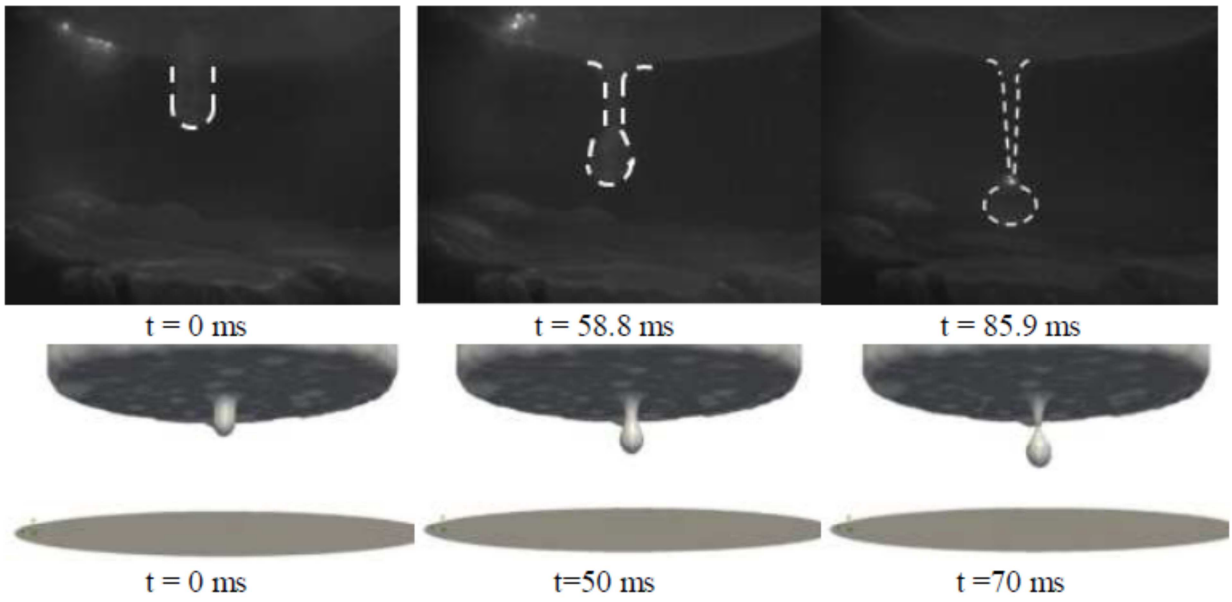

Figure 4. Formation and detachment of a drop observed experimentally (top row) and predicted by the numerical model (bottom row).

The dimension of the simulated drop is of the same order of magnitude (around 1 cm) as that of the actual drop. It is also interesting to note that the characteristic times for each stage are of the same order of magnitude, even if the "numerical" drop takes less time to detach than in reality. Although this comparison can only be qualitative since the simulation does not take into account the electromagnetic effects related to the presence of the arc, the simulated behavior remains close to the experimental visualizations.

Fluid flow inside a protuberance

As an example of the typical fluid flow present in the protuberance, Fig. 5 shows the computed streamlines and velocity vectors in a vertical plane crossing a protuberance. The two white lines represent the free surface of the liquid film and the liquid/solid interface respectively. The fluid flow is governed by the drainage of the liquid film as well as buoyancy forces. It is characterized by a large recirculation loop that occupies the whole volume of the protuberance. The velocity magnitude reaches a maximum value of around 20 $cm.s^{-1}$ located on the central axis of the protuberance (Fig. 5.c).

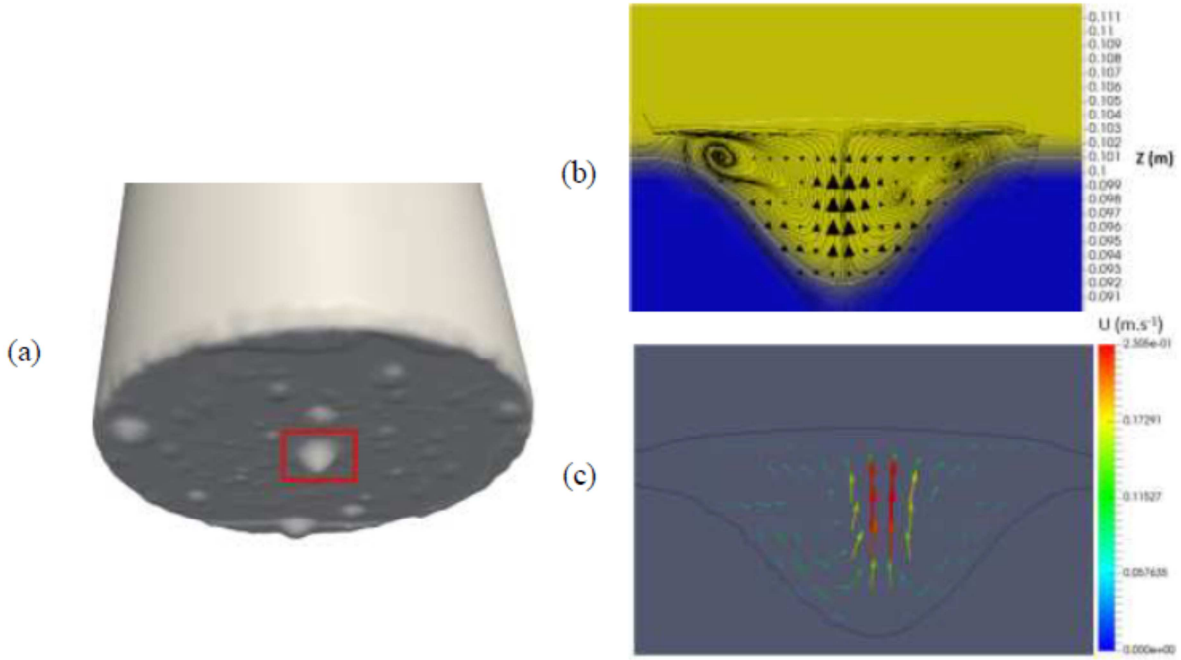

Figure 5. Streamlines and velocity vectors inside a protuberance.

Heat transfer in the electrode

The computed temperature field in a vertical cutting plane of the electrode at t = 707 s is presented in Fig. 6.a, with the initial state of the electrode represented by white dashed lines. The temperature profile along the electrode axis at the same time is plotted in Fig. 6.b. Due to the consumption of the electrode, the power supplied by the electric arc affects mainly a small region at the electrode tip as shown in the Fig. 6.a. This region, usually referred to as the "heat affected zone", is about 10 centimeters high. This behavior is in a good agreement with the experimental observations of El Mir et al. [21]. In the absence of consideration of thermal losses by radiation at the electrode lateral wall, the temperature remains essentially uniform in the horizontal direction. Note that the temperature of the liquid film exceeds the liquidus temperature with a superheat reaching around 100 °C.

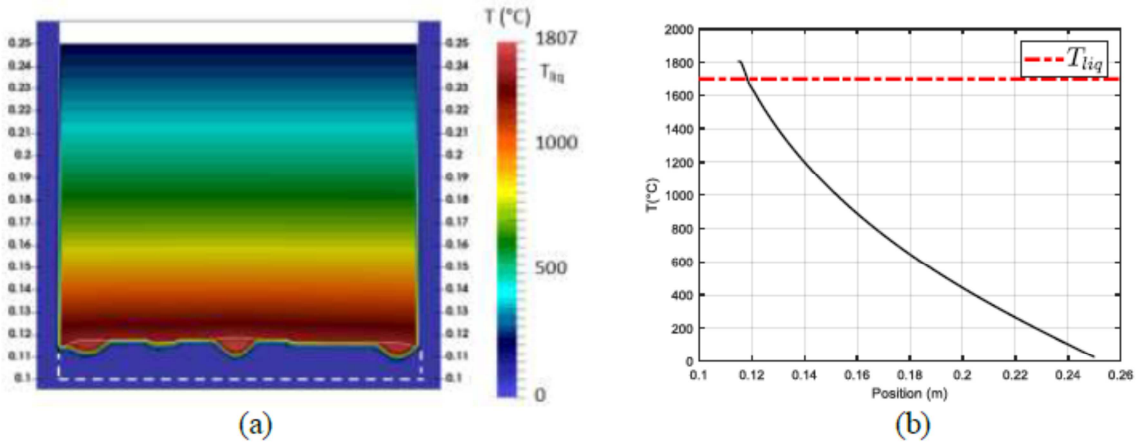

Figure 6. (a) Temperature field in the electrode at t = 707 s, (b) Temperature profile along the electrode revolution axis.

Predicted melt rate

The time evolution of the electrode melt rate, calculated from the evolution of the electrode mass, is plotted in Fig. 7. The electrode begins effectively to melt after a pre-heating stage of around 10 min. The variation of the melt rate is characterized by a sharp increase until reaching a quasi-stationary regime. The average calculated melt rate is 0.96 kg.min^{-1} with fluctuations between 0.75 and 1.3 kg.min^{-1}. In the current model, it should be noted that the process starts at full power, contrary to the real process in which the electric current is gradually increased.

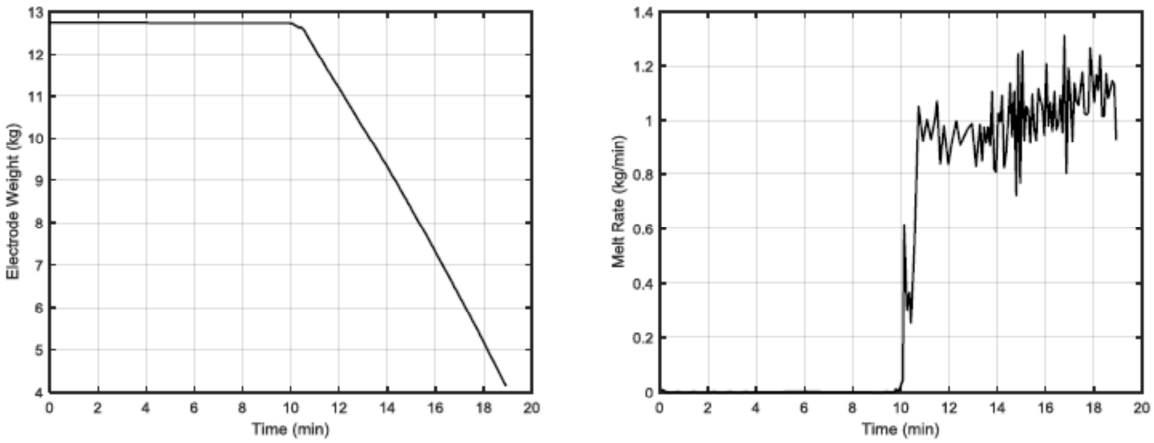

(a) (b)

Figure 7. Time variation of the predicted melt rate (b) from the electrode weight variation (a)

Conclusion

A 3D numerical model was developed in order to simulate the melting of a VAR consumable electrode. This work couples the enthalpy-porosity approach to simulate the melting process and the volume of fluid method to model the deformation of the liquid film formed under the electrode. Simulation results applied to the melting of a small diameter electrode with a large interelectrode gap have been presented, illustrating the formation and dripping of the liquid film and the thermal behavior of the electrode. The results of the simulation were found to be in good qualitative agreement with experimental observations reported in the literature. The model enables also to predict the electrode overall melt rate.

In the future, the present model will be further improved by adding a description of the thermal losses by radiation at the electrode lateral wall. In addition, simulations will be performed for the case of an industrial steel electrode. This differs from the case presented in this paper by the much larger dimension of the electrode as well as the much smaller interelectrode gap (typically around 10 mm). The latter is responsible for a radically different mode of transfer of the liquid metal (involving drip-shorts instead of fully detached drops).

Acknowledgments

The authors would like to thank Y. Millet and J. Jourdan from TIMET Savoie, France, who have supported the acquisition of the experimental data shown in fig. 4 of the present work.

References

1. Yu K-O (2001) Modeling for casting and solidification processing. CRC Press

2. Yu KO, Domingue J (1989) control of solidification structure in VAR and ESR processed alloy 718 ingots. Superalloy 718 Metall Appl 33–48

3. Zanner FJ, Bertram LA, Adasczik C, O'Brien T (1984) Observations of melt rate as a function of arc power, CO pressure, and electrode gap during vacuum consumable arc remelting of Inconel 718. Metall Trans B 15:117–125

4. Williamson RL, Zanner FJ, Grose SM (1997) Arc voltage distribution properties as a function of melting current, electrode gap, and CO pressure during vacuum arc remelting. Metall Mater Trans B 28:841–853

5. Zanner FJ (1979) Metal transfer during vacuum consumable arc remelting. Metall Trans B 10:133–142

6. Chapelle P, Noël C, Risacher A, et al (2016) Characterization of the behaviour of the electric arc during VAR of a Ti alloy. In: IOP Conference Series: Materials Science and Engineering. IOP Publishing, p 012011

7. Jardy A, Ablitzer D (2006) Solar: numerical software to optimize vacuum arc remelting operations. Xiyou Jinshu Cailiao Yu GongchengRare Met Mater Eng 35:119–122

8. Kelkar KM, Patankar SV, Mitchell A, et al (2007) Computational modeling of the Vacuum Arc Remelting (VAR) process used for the production of ingots of Titanium alloys. In: 11th World Conference on Titanium (Ti-2007), Kyoto, Japan, June. pp 3–7

9. Pericleous K, Djambazov G, Ward M, et al (2013) A multiscale 3D model of the vacuum arc remelting process. Metall Mater Trans A 44:5365–5376

10. Voller VR, Prakash C (1987) A fixed grid numerical modelling methodology for convection-diffusion mushy region phase-change problems. Int J Heat Mass Transf 30:1709–1719

11. Hirt CW, Nichols BD (1981) Volume of fluid (VOF) method for the dynamics of free boundaries. J Comput Phys 39:201–225

12. H.Rusche (2002) Computational fluid dynamics of dispersed two-phase flows at high phase fractions. PhD thesis

13. Brackbill JU, Kothe DB, Zemach C (1992) A continuum method for modeling surface tension. J Comput Phys 100:335–354

14. Ubbink O (1997) Numerical prediction of two fluid systems with sharp interfaces

15. Harvie DJ, Davidson MR, Rudman M (2005) An analysis of parasitic current generation in volume of fluid simulations. ANZIAM J 46:133–149

16. Brent AD, Voller VR, Reid KTJ (1988) Enthalpy-porosity technique for modeling convection-diffusion phase change: application to the melting of a pure metal. Numer Heat Transf Part Appl 13:297–318

17. Issa RI (1986) Solution of the implicitly discretised fluid flow equations by operator-splitting. J Comput Phys 62:40–65

18. Patankar S (1980) Numerical heat transfer and fluid flow. CRC press

19. Chandrasekhar (1961) Hydrodynamic and hydromagnetic stability

20. Limat L, Giorgiutti F, Fermigier M, et al (1997) Dynamique non-linéaire d'instabilités de surface: gouttes et colonnes liquides formées par ruissellement de films. Rev Générale Therm 36:672–681

21. Mir HE, Jardy A, Bellot J-P, et al (2010) Thermal behaviour of the consumable electrode in the vacuum arc remelting process. J Mater Process Technol 210:564–572. https://doi.org/10.1016/j.jmatprotec.2009.11.008